# Multiphase lattice Boltzmann method for particle suspensions

Abhijit S. Joshi and Ying Sun*

*State University of New York at Binghamton, Binghamton, New York 13902, USA*
(Received 3 December 2008; published 4 June 2009)

A two-dimensional mass conserving lattice Boltzmann method (LBM) has been developed for multiphase (liquid and vapor) flows with solid particles suspended within the liquid and/or vapor phases. The main modification to previous single-phase particle suspension models is the addition of surface (adhesive) forces between the suspended particle and the surrounding fluid. The multiphase dynamics between fluid phases is simulated via the single-component multiphase model of Shan and Chen [Phys. Rev. E **47**, 1815 (1993)]. The combined multiphase particle suspension model is first validated and then used to simulate the dynamics of a single-suspended particle on a planar liquid-vapor interface and the interaction between a single particle and a free-standing liquid drop. It is observed that the dynamics of suspended particles near free-standing liquid droplets is affected by spurious velocity currents although the liquid-vapor interface itself is a local energy minimum for particles. Finally, results are presented for capillary interactions between two suspended particles on a liquid-vapor interface subjected to different external forces and for spinodal decomposition of a liquid-vapor mixture in the presence of suspended particles. Qualitative agreements are reached when compared with results of suspended particles in a binary mixture based on multicomponent LBM models.

## I. INTRODUCTION

Using the lattice Boltzmann method (LBM) to study suspensions of solid particles in a single-phase fluid was pioneered by Ladd [1,2]. Over the years, it has attracted great interest within the LBM research community and several versions of the original algorithm are now available [3–8]. The LBM model for suspensions has been proven to be a promising simulation tool in applications ranging from colloidal suspensions [9,10] to biofluids [11] and shows very good scaling on large-scale parallel computing platforms with up to a million particles [12]. On another front, there has been a rapid development of multiphase and multicomponent LBM models [13–18]. However, combining these two research endeavors has not been pursued until very recently [19–21]. These recent efforts have focused on the motion of suspended particles in the interface or bulk regions of multicomponent fluids, having similar densities.

In this paper, we report some results of combining the Shan and Chen single-component multiphase (SCMP) model with a model for particle suspensions for a system composed of liquid and vapor, with suspended particles in one or both of the fluid phases. A unique challenge of this approach is to accurately model the coexistence of at least three phases (liquid, vapor, fixed solid walls, and/or moving suspended particles). Unlike the multicomponent LBM, the multiphase LBM involves (a) large density ratio between fluid (liquid and vapor) phases and (b) less flexibility in independently varying the interface tensions between the liquid, vapor, and solid phases due to the strong correlation between the interface tension and cohesive/adhesive forces. Modifications made in the LBM algorithm to make the model mass conserving and stable are the following:

(i) Treatment of interior fluid nodes inside the suspended particles. Like the original motivation given by Ladd [1,2],

the interior fluid inside particles is maintained to avoid creating and destroying fluid at nodes as the particle moves on the lattice. Thus, unlike methods where the internal fluid is completely removed [3], the problem of initializing newly created fluid nodes (originally inside the moving particle) does not arise and the mass of the entire system is exactly conserved. The collision, streaming, and bounce-back steps in the LBM algorithm (described in detail in Secs. II and III) are carried out even in this interior fluid, with some minor changes that will be described later. However, the velocity at interior fluid nodes is always reset to the particle velocity assuming that the entire fluid phase inside a particle moves like a rigid body with the same velocity as that of the particle itself. Collisions of the interior fluid with the particle boundary do not contribute directly to the force calculations on the suspended particle, similar to the *virtual fluid* used in Ding and Aidun [8]. However, it influences the force calculation indirectly when the particle representation on the LBM lattice changes. Finally, following Heemels *et al.* [7], we eliminate the effect of sound propagation in the interior fluid by averaging and redistributing the density.

(ii) Inclusion of adhesive forces acting on the suspended particles. Adhesive forces between the external fluid (outside suspended particles) on the suspended particle are introduced such that they are equal and opposite to the adhesive forces exerted by the solid on the fluid. These forces are not present for the internal fluid (inside particles). These forces can be used to control the wetting properties of suspended particles relative to the liquid-vapor interface.

The subsequent part of the paper is organized as follows. In Sec. II, the Shan and Chen multiphase model is summarized. Section III gives a detailed discussion of the particle suspension model. Section IV describes several validation cases for individual submodels. The combined (multiphase +particle suspension) model is then used in Sec. V to simulate various problems where the suspended particles are confined within the liquid/vapor or are present in both phases. The model and results are summarized in Sec. VI. Envi-

---

*ysun@binghamton.edu

sioned applications of the model are to predict the wetting, dewetting, contact line pinning, and particle self-assembly of a drop containing colloidal particles as it spreads on various types of surface energy heterogeneous and/or rough substrates.

## II. MULTIPHASE LATTICE BOLTZMANN METHOD

The LBM can be viewed as a discrete approximation of the Boltzmann equation [22]. But in most implementations, the LBM is an alternative computational fluid-dynamics approach for solving the Navier-Stokes equations, which can be derived from the LBM using the Chapman-Enskog procedure [23] or an asymptotic expansion technique [24]. This section is a brief summary of the isothermal two-phase (liquid+vapor) LBM model introduced by Shan and Chen [14]. The LBM simulates fluid flow on a discrete lattice with equally spaced nodes along the $x$ and $y$ directions represented by square symbols in Fig. 1(a). The primary dependent variables at each node are the particle velocity distribution functions (PDFs) along different lattice directions ($\alpha$). The PDF along a certain direction represents the number of fluid particles moving in that direction at that time and is indicated by $f_\alpha$. The transport of these PDFs along discrete lattice directions and their interactions via suitably designed collision terms can reproduce the dynamics of the Navier-Stokes equations. At any lattice node $\mathbf{x}$, the evolution of the PDF with time $t$ is governed by the lattice Boltzmann equation given by

$$f_\alpha(\mathbf{x}+\mathbf{e}_\alpha, t+1) = f_\alpha(\mathbf{x},t) - \left\{ \frac{f_\alpha(\mathbf{x},t) - f_\alpha^{eq}[\rho(\mathbf{x},t), \mathbf{u}(\mathbf{x},t)]}{\tau} \right\} \\ + f_\alpha^{eq}[\rho(\mathbf{x},t), \tilde{\mathbf{u}}(\mathbf{x},t)] - f_\alpha^{eq}[\rho(\mathbf{x},t), \mathbf{u}(\mathbf{x},t)].$$

(1)

The right-hand side in Eq. (1) represents the collision step and equating the right-hand side to the left-hand side represents the streaming step. The relaxation time in Eq. (1) controls the kinematic viscosity $\nu$ of the lattice Boltzmann fluid via the relationship $\nu=(2\tau-1)/6$. All equations in this work are presented in *lattice units*, where the lattice spacing along the $x$ and $y$ axes and the time step are all unity ($\Delta x=\Delta y=\Delta t=1$). The LBM results can be compared with experiments or with other theoretical/numerical results via the calculation of suitable dimensionless numbers. The fundamental principle used is that dimensionless numbers are the same in lattice units and physical units. Examples of such comparisons are given later in Secs. IV A and IV C. Note that the last two terms in Eq. (1) are the result of using the exact difference method (EDM) introduced by Kupershtokh and Medvedev [25]. The EDM ensures that the density ratio between the liquid and vapor phases is not affected when the relaxation time $\tau$ is different than unity or when different values of $\tau$ are used in the liquid and vapor phases.

The discrete velocities $\mathbf{e}_\alpha$ depend on the particular velocity model used and we use the D2Q9 model that has nine velocity directions ($\alpha=0$ to 8) at a given lattice point, with the individual components along the $x$ and $y$ directions given by
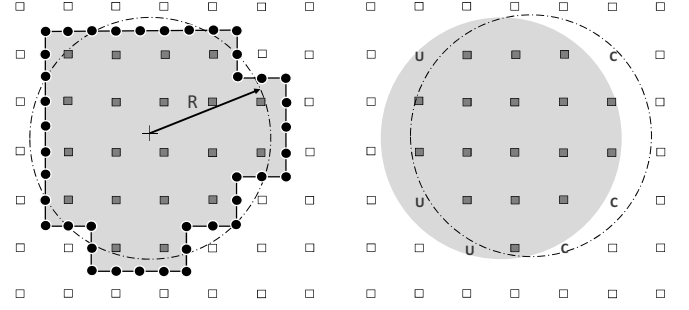


FIG. 1. (a) Mapping of a circular particle of radius $R$ (dashed line) on the LBM lattice, showing external fluid nodes (white squares) and internal fluid nodes (dark squares). The shaded region is the effective shape of the particle. The fluid interacts with the particle at the boundary nodes (black circles). (b) Change in the particle representation on the lattice during one lattice time step, with the shaded circle representing the previous location and the dashed circle representing the new location. Some internal fluid nodes are uncovered ($U$) and become external fluid nodes, while some external fluid nodes are covered ($C$) by the particle and become internal fluid nodes.

$$\mathbf{e}_0 = (0,0), \quad \mathbf{e}_1 = (1,0), \quad \mathbf{e}_2 = (1,1),$$

$$\mathbf{e}_3 = (0,1), \quad \mathbf{e}_4 = (-1,1), \quad \mathbf{e}_5 = (-1,0),$$

$$\mathbf{e}_6 = (-1,-1), \quad \mathbf{e}_7 = (0,-1), \quad \mathbf{e}_8 = (1,-1). \quad (2)$$

The macroscopic density $\rho$ and velocity $\mathbf{u}$ at each fluid node are obtained using

$$\rho = \sum_{\alpha=0}^{8} f_\alpha, \quad (3)$$

$$\rho\mathbf{u} = \sum_{\alpha=1}^{8} f_\alpha \mathbf{e}_\alpha. \quad (4)$$

These macroscopic quantities are used to evaluate the equilibrium PDF $f_\alpha^{eq}$ given by

$$f_\alpha^{eq}(\rho,\mathbf{u}) = \rho w_\alpha \left[ 1 + 3(\mathbf{e}_\alpha \cdot \mathbf{u}) + \frac{9}{2}(\mathbf{e}_\alpha \cdot \mathbf{u})^2 - \frac{3}{2}(\mathbf{u} \cdot \mathbf{u})^2 \right].$$

(5)

The weight functions for different directions are $w_0=4/9$, $w_\alpha=1/9$ for $\alpha=1,3,5,7$ and $w_\alpha=1/36$ for $\alpha=2,4,6,8$. The modified velocity $\tilde{\mathbf{u}}$ to account for particle interactions, as introduced in Shan and Chen [14] and modified by Kupershtokh and Medvedev [25], is given by

$$\tilde{\mathbf{u}} = \mathbf{u} + \frac{1}{\rho}(\mathbf{F}_{cohesive} + \mathbf{F}_{adhesive} + \mathbf{F}_{body}). \quad (6)$$

The modified velocity $\tilde{\mathbf{u}}$ from Eq. (6) replaces $\mathbf{u}$ in Eq. (4) while calculating the equilibrium function in the third term on the right-hand side of Eq. (1). Finally, the actual fluid velocity $\mathbf{u}'$ (used for plotting velocity vector fields) is the average velocity before and after the collision event and is given by

$$\mathbf{u}' = \mathbf{u} + \frac{1}{2\rho}(\mathbf{F}_{cohesive} + \mathbf{F}_{adhesive} + \mathbf{F}_{body}). \quad (7)$$

The cohesive force at location $\mathbf{x}$ arises because of the attraction between fluid particles at $\mathbf{x}$ and fluid particles at neighboring locations $\mathbf{x} + \mathbf{e}_\alpha$. This attraction is proportional to the effective density [14], $\Psi(\mathbf{x}) = \Psi[\rho(\mathbf{x})] = 1 - \exp(-\rho)$, at interacting nodes and is calculated using

$$\mathbf{F}_{cohesive}(\mathbf{x}) = -\sum_{\alpha=1}^{8} G_\alpha^{fluid\text{-}fluid} \Psi(\mathbf{x}) \Psi(\mathbf{x} + \mathbf{e}_\alpha) \mathbf{e}_\alpha. \quad (8)$$

For the D2Q9 model, $G_\alpha^{fluid\text{-}fluid} = g_f$ for $\alpha = 1, 3, 5, 7$ and $G_\alpha^{fluid\text{-}fluid} = g_f/4$ for $\alpha = 2, 4, 6, 8$. If the interparticle cohesive force parameter $g_f$ is negative, attractive forces are set up between fluid at neighboring nodes on the lattice and this leads to the formation of a high-density liquid phase surrounded by a low-density vapor phase. Larger values of $|g_f|$ correspond to greater attractive forces, leading to higher-density ratios between the liquid and vapor phases. Care must be taken while using the expression in Eq. (8) near solid walls (or near suspended particles). In such a case, we use a wall density value ($\rho_w = \rho_c = 0.693$) for the solid node (or the fluid node inside the suspended particle) and set $\rho = \rho_w$ to calculate the effective density $\Psi$ at the solid node [26]. Thus, an adhesive force is introduced between the fluid and solid nodes (independent of the adhesive force discussed next). The wetting behavior of a liquid drop in contact with a solid wall can be controlled entirely by adjusting this wall density. We find that using $\rho_w = 0.693$ ensures that the contact angle is close to 90° when the adhesive force parameter $g_w$ to be discussed later is set to zero. The pressure $P$ can be obtained using the equation of state (EOS). For the D2Q9 model, the EOS is given by [25]

$$P = \frac{\rho}{3} + \frac{3}{2} g_f \Psi^2. \quad (9)$$

The speed of sound $c_s = 1/\sqrt{3}$ and the critical density is $\rho_c = 0.693$. Phase separation occurs when $g_f < -4/9$. The equation of state can be changed by modifying the expression for an effective density [27].

We control the degree of departure of the contact angle from 90° via an additional adhesive force given by

$$\mathbf{F}_{adhesive}(\mathbf{x}) = -\sum_{\alpha=1}^{8} G_\alpha^{fluid\text{-}solid} \rho(\mathbf{x}) \rho(\mathbf{x} + \mathbf{e}_\alpha) \mathbf{e}_\alpha. \quad (10)$$

For the D2Q9 model, $G_\alpha^{fluid\text{-}solid} = g_w$ for $\alpha = 1, 3, 5, 7$ and $G_\alpha^{fluid\text{-}solid} = g_w/4$ for $\alpha = 2, 4, 6, 8$. The function $\rho_s(\mathbf{x} + \mathbf{e}_\alpha) = 1$ if the location $\mathbf{x} + \mathbf{e}_\alpha$ corresponds to a solid node (or a fluid node inside suspended particles) and $\rho_s(\mathbf{x} + \mathbf{e}_\alpha) = 0$ otherwise. Thus, the adhesive force is present only if one or more of the neighbors of a fluid node at location $\mathbf{x}$ is solid. The magnitude of the adhesive force is controlled by the parameter $g_w$, with positive values of $g_w$ leading to repulsive forces (nonwetting behavior) and negative values of $g_w$ leading to attractive forces (wetting behavior). Note that the fluid sticks to the wall even when $g_w = 0$ because of the cohesive attraction

between the solid node and the adjacent fluid node, as discussed in the previous paragraph.

The interaction force-based multiphase model leads to the development of spurious velocity currents [based on Eq. (7)] close to the liquid-vapor interface, when the interface curvature is nonzero. In general, the magnitude of these currents $|\mathbf{u}_s|_{max}$ increases with the density ratio $\rho_L/\rho_V$ between the liquid and vapor phases. Our computations for liquid drops show that $|\mathbf{u}_s|_{max} = 0.0046$ for $\rho_L/\rho_V = 10$ and $|\mathbf{u}_s|_{max} = 0.0265$ for $\rho_L/\rho_V = 30$. The presence of these currents can significantly influence the motion of suspended particles close to the interface, as shown later in Sec. V B. For a given density ratio, these spurious currents can also be reduced by incorporating additional rings of neighboring nodes while calculating adhesive and cohesive interactions [28].

## III. PARTICLE SUSPENSION MODEL

For simplicity, the suspended particles (hereafter referred to as simply "particles") are circular in shape and the location of each particle, the particle radii, and the linear and angular velocities are specified as part of the initial conditions. To allow the particle to interact with the LBM, nodes inside and outside the particle are identified as shown in Fig. 1(a). Boundary nodes are located half way between fluid nodes inside the particle and external fluid nodes. As the particle moves, this mapping is updated. Initially, nodes lying in the liquid phase are assigned the liquid density and nodes in the vapor phase are assigned the vapor density, corresponding to the value of the cohesive force parameter $g_f$. Note that the fluid phase is present at all nodes in the domain, except fixed solid nodes, if any. The fluid velocity is initially set to zero at all nodes unless otherwise specified. After initialization, each time step involves the following substeps:

(1) Updating particle positions based on the forces and torques acting on each particle.

(2) Calculation of forces and torques due to the change in particle representation on the lattice.

(3) Calculation of equilibrium distributions.

(4) Streaming (includes bounce back at fixed walls and at moving particle interfaces).

(5) Updating the force and torque on each particle.

(6) Updating macroscopic variables (density and velocity) in the fluid phase.

In the following, each of the above steps is presented in detail.

### A. Particle dynamics and kinematics

This step is made up of two substeps. The first substep is dynamics, where Newton's second law of motion is applied to each individual particle to calculate the changes in the linear and angular velocities ($\mathbf{U}_p$ and $\Omega_p$, respectively) because of the total force $\mathbf{F}^p$ and total torque $\mathbf{T}^p$ acting on it, using

$$\mathbf{F}^p = M_p \frac{d}{dt} \mathbf{U}_p, \quad (11)$$

$$\mathbf{T}^p = I_p \frac{d}{dt} \Omega_p. \tag{12}$$

For an explicit update, the linear velocity at the new time level $(n+1)$ is obtained using forces calculated at the previous time level $(n)$ and the discrete version of Eq. (11) is given by $\mathbf{U}_p^{n+1} = \mathbf{U}_p^n + \mathbf{F}^{p,n}/M_p$. A similar expression can be used to update the angular velocity. However, an explicit update of the linear and angular velocities (especially the latter) based on Eqs. (11) and (12) is unstable for low particle densities. This problem can be avoided by using an implicit update [6] (Appendix). For the explicit update, we follow Ladd [1] and use time averaging over two successive time steps to calculate the forces. We assign a solid density to the particles and use the following relationships to determine the mass and moment of inertia for a particle of density $\rho_p$ and radius $R$:

$$M_p = \rho_p \pi R^2, \tag{13}$$

$$I_p = \frac{1}{2} \rho_p R^2. \tag{14}$$

The total force $\mathbf{F}^p$ in Eq. (11) is composed of the forces due to the changing representation of the particle on the lattice ($\mathbf{F}_C^p$ and $\mathbf{F}_U^p$), force due to the momentum transfer from the fluid $\mathbf{F}_{bbk}^p$, adhesive force $\mathbf{F}_{adh}^p$, and lubrication and Hookean forces (acting between pairs of particles) denoted by $\mathbf{F}_{lub}^p$ and $\mathbf{F}_{Hook}^p$, respectively (superscript $p$ denotes that the force is acting on the particle). Thus,

$$\mathbf{F}^p = \mathbf{F}_C^p + \mathbf{F}_U^p + \mathbf{F}_{bbk}^p + \mathbf{F}_{adh}^p + \mathbf{F}_{lub}^p + \mathbf{F}_{Hook}^p. \tag{15}$$

Similarly, the total torque is obtained using

$$\mathbf{T}^p = \mathbf{T}_C^p + \mathbf{T}_U^p + \mathbf{T}_{bbk}^p + \mathbf{T}_{adh}^p. \tag{16}$$

Lubrication and Hookean forces are assumed to act along a line connecting the centers of mass of the involved particle pairs and therefore do not contribute to the torque. The calculation of all these forces and torques is discussed in Secs. III B and III E.

The next substep is kinematics, where the updated linear and angular velocities are used to calculate the new position and angular orientation of each particle, the latter being redundant if the particles are circular. Note that although particle positions and velocities are updated continuously in time as their dynamics evolves, the representation of the particle on the discrete LBM lattice may not change at every time step.

### B. Force and torque due to changing particle representation on the lattice

When the particle moves from one time level to the next, it may cover some nodes that were formerly external fluid nodes. These nodes are indicated in Fig. 1(b) by the letter $C$ and their location at the new time level is denoted by $\mathbf{r}_C$. The center of mass of the particle at the *new* time level is denoted by $\mathbf{R}$. In such a case, the momentum at these fluid nodes is transferred to the particle and the resultant force and torque on the particle can be calculated using

$$\mathbf{F}_C^p = \sum_C \rho_C \mathbf{u}_C \tag{17}$$

and

$$\mathbf{T}_C^p = \sum_C (\mathbf{r}_C - \mathbf{R}) \times \rho_C \mathbf{u}_C. \tag{18}$$

The density and velocity values from the previous time step (when node $C$ was an external fluid node) are used in Eqs. (17) and (18).

Similarly, some nodes that were originally inside the particle can be uncovered and become external fluid nodes. These are indicated in Fig. 1(b) by the letter $U$ and are located at $\mathbf{r}_U$ at the old time level. The center of mass of the particle at the *old* time level is $\mathbf{R}$. In this case, the momentum corresponding to the fluid motion is lost by the particle and the resultant force and torque on the particle are obtained using

$$\mathbf{F}_U^p = -\sum_U \bar{\rho}_U \mathbf{u}_U \tag{19}$$

and

$$\mathbf{T}_U^p = -\sum_U (\mathbf{r}_U - \mathbf{R}) \times \bar{\rho}_U \mathbf{u}_U. \tag{20}$$

The density $\bar{\rho}_U$ represents the average density of the fluid inside the particle at the previous time step (when the node $U$ was part of the interior fluid) and the velocity corresponds to the rigid-body motion of the particle at the previous time level, as discussed later in Sec. III F. Unlike schemes that do not use the interior fluid at all [3], no extrapolations are required in the present model to assign density and velocity to nodes uncovered by the moving particle and mass is therefore exactly conserved. If the particle representation on the lattice does not change from one time level to the next, the forces and torques in this section are zero.

### C. Calculation of equilibrium distributions

The density and velocity at each node point (including fluid nodes inside the suspended particles) are used to calculate the equilibrium distributions given in Eq. (5). As discussed in Sec. III F, the fluid velocity inside each particle is reset to correspond to the rigid-body motion of the particle as a whole. This modified velocity is used to calculate equilibrium distributions for fluid nodes inside the particle. The density of fluid inside the particle is reset to the average value. This average density is used to calculate equilibrium functions for fluid nodes inside suspended particles. In the fluid outside the suspended particle, the velocity used in the equilibrium function is given by Eqs. (4) and (6). Care should be taken to include the cohesive and adhesive force terms while calculating the modified velocity at (external)

fluid nodes adjacent to the suspended particle, similar to the case where fluid nodes are adjacent to a fixed solid wall.

### D. Streaming and bounce back at fixed and moving solid boundaries

The *postcollision* PDF $f_\alpha^+$ at lattice node $\mathbf{x}$ along direction $\alpha$ is the right-hand side of Eq. (1) and is defined as

$$f_\alpha^+ = f_\alpha(\mathbf{x},t) - \left\{ \frac{f_\alpha(\mathbf{x},t) - f_\alpha^{eq}[\rho(\mathbf{x},t),\mathbf{u}(\mathbf{x},t)]}{\tau} \right\}$$
$$+ f_\alpha^{eq}[\rho(\mathbf{x},t),\tilde{\mathbf{u}}(\mathbf{x},t)] - f_\alpha^{eq}[\rho(\mathbf{x},t),\mathbf{u}(\mathbf{x},t)]. \quad (21)$$

It is $f_\alpha^+$ that will now stream to the adjacent lattice point $\mathbf{x} + \mathbf{e}_\alpha$. The streaming step from a fluid node (outside the particle) to a neighboring fluid node (also outside the particle) can be described as

$$f_\alpha(\mathbf{x} + \mathbf{e}_\alpha, t+1) = f_\alpha^+. \quad (22)$$

Physically, this process can be thought of as a movement of fluid particles from location $\mathbf{x}$ to location $\mathbf{x} + \mathbf{e}_\alpha$. If the adjacent node corresponds to a fixed solid node, the half-way bounce-back scheme is used to simulate the no-slip boundary condition. The streaming step at these nodes can be described as

$$f_{\bar{\alpha}}(\mathbf{x}, t+1) = f_\alpha^+, \quad (23)$$

where the direction $\bar{\alpha}$ is defined to be the direction opposite to $\alpha$. The no-slip boundary is effectively present at a location midway between the fluid node and the fixed solid node.

Finally, we consider the case where streaming occurs from a fluid node just outside a (moving) particle toward a node that is inside the particle. Based on the (known) particle velocity, we first determine the velocity of the *boundary node* assumed to be located midway between the fluid node and the node inside the particle and indicated by the filled circle in Fig. 1(a). The boundary node *velocity* includes both translational and rotational components of the particle velocity and is given by

$$\mathbf{u}_b = \mathbf{U} + \mathbf{\Omega} \times (\mathbf{r}_b - \mathbf{R}), \quad (24)$$

where $\mathbf{U}$ is the translational velocity of the particle, $\mathbf{\Omega}$ is the angular velocity, $\mathbf{r}_b$ is the location of the boundary node, and $\mathbf{R}$ is the location of the center of mass of the particle. The streaming step can now be described as

$$f_{\bar{\alpha}}(\mathbf{x}, t+1) = f_\alpha^+ - 6\rho_w w_\alpha(\mathbf{u}_b \cdot \mathbf{e}_\alpha). \quad (25)$$

Note that if the boundary node velocity is zero, Eq. (25) reduces to the conventional bounce-back rule. There is a small *change in mass* associated with the modified bounce-back rule in Eq. (25) because of the second term on the right-hand side. This can be exactly compensated by using a similar bounce-back rule for the fluid inside the suspended particle and using the same *wall density* for both cases. In this work, we set $\rho_w$ to be the density at the external fluid node.

If the surfaces of two particles are closer than one lattice spacing along a certain link, there are no (external) fluid

nodes separating them along that link. To ensure mass conservation, streaming along this link from the interior fluid in each particle is carried out assuming that the neighboring fluid node (inside the other particle) is a fixed solid node. It must be mentioned that accurate LBM schemes have been devised to implement the no-slip boundary for curved moving boundaries [29–33]. However, most of these schemes suffer from an inability to conserve mass because of the interpolations used. We have chosen to use the half-way bounce back rule both for simplicity and in order to maintain a mass imbalance close to machine zero.

### E. Updating the force and torque on each particle

At each boundary node point $\mathbf{x}$ in the external fluid (along the direction $\mathbf{e}_\alpha$, where $\mathbf{x} + \mathbf{e}_\alpha$ is an internal fluid node), a hydrodynamic force is exerted because of the change in momentum of the fluid particles impinging along $\mathbf{e}_\alpha$ (represented by $f^+$) and getting reflected back along $\mathbf{e}_{\bar{\alpha}}$ [represented by $f_\alpha^+ - 6\rho_w w_\alpha(\mathbf{u}_b \cdot \mathbf{e}_\alpha)$]. The total force and torque on the particle are calculated by summing these interactions along all boundary nodes ($bn$) and along all relevant directions for each boundary node using

$$\mathbf{F}_{bbk}^p = \sum_{bn} \sum_\alpha [2f_\alpha^+ - 6\rho_w w_\alpha(\mathbf{u}_b \cdot \mathbf{e}_\alpha)]\mathbf{e}_\alpha \quad (26)$$

and

$$\mathbf{T}_{bbk}^p = \sum_{bn} (\mathbf{r}_{bn} - \mathbf{R}) \sum_\alpha [2f_\alpha^+ - 6\rho_w w_\alpha(\mathbf{u}_b \cdot \mathbf{e}_\alpha)]\mathbf{e}_\alpha. \quad (27)$$

Similarly, the total adhesive force acting on the particle can be obtained by adding up the adhesive force contributions at all boundary nodes and along all relevant directions at each boundary node. The adhesive force and torque acting on the particle is given by

$$\mathbf{F}_{adh}^p = \sum_{bn} \sum_\alpha [G_\alpha^{fluid\text{-}fluid}\Psi(\mathbf{x})\Psi(\mathbf{x} + \mathbf{e}_\alpha)\mathbf{e}_\alpha$$
$$+ G_\alpha^{fluid\text{-}solid}\rho(\mathbf{x})\rho(\mathbf{x} + \mathbf{e}_\alpha)\mathbf{e}_\alpha] \quad (28)$$

and

$$\mathbf{T}_{adh}^p = \sum_{bn} (\mathbf{r}_{bn} - \mathbf{R}) \sum_\alpha [G_\alpha^{fluid\text{-}fluid}\Psi(\mathbf{x})\Psi(\mathbf{x} + \mathbf{e}_\alpha)\mathbf{e}_\alpha$$
$$+ G_\alpha^{fluid\text{-}solid}\rho(\mathbf{x})\rho(\mathbf{x} + \mathbf{e}_\alpha)\mathbf{e}_\alpha]. \quad (29)$$

The density values used in Eqs. (28) and (29) are exactly identical to those used while calculating the adhesive and cohesive forces on the (external) fluid because of the particle.

If the distance $h$ between the surfaces of two suspended particles 1 and 2 (of radii $a_1$ and $a_2$) is small, there are insufficient (external) fluid nodes between the moving surfaces to resolve the lubrication forces. To correctly model this effect in the LBM, additional forces must be introduced between each such pair of particles when their respective surfaces get closer than a certain cut-off distance $h_c$. For the two-dimensional (2D) case, we use the expression derived by Kromkamp *et al.* [10] to model the lubrication force between a pair of interacting cylinders. The force on particle 1 is given by

$$\mathbf{F}_{lub}^{p} = \mathbf{0}, h \geq h_{c},$$

$$\mathbf{F}_{lub}^{p} = -\frac{1}{2}\mu \mathbf{U}_{12} \cdot \hat{\mathbf{R}}_{12}\left[\left(\frac{a_1 + a_2}{h}\right)^{3/2}\left(F_0 + \frac{h}{a_1 + a_2}F_1\right)\right.$$
$$\left. - \left(\frac{a_1 + a_2}{h_c}\right)^{3/2}\left(F_0 + \frac{h_c}{a_1 + a_2}F_1\right)\right], h < h_c. \quad (30)$$

In Eq. (30), $\hat{\mathbf{R}}_{12}$ is the unit vector from the center of particle 1 toward particle 2, $\mathbf{U}_{12}$ is the velocity of particle 2 relative to particle 1, $\mu$ is the dynamic viscosity, and the constants are $F_0 = 3\pi\sqrt{2}/4$ and $F_1 = 231\pi\sqrt{2}/80$. The critical spacing used is $h_c = 2$. Note that Eq. (30) is applied pairwise to all particles whose outer surfaces are within the cut-off distance from each other.

In addition to the lubrication force, we introduce a Hookean repulsion between particles, identical to that used in Kromkamp *et al.* [10] if their respective surfaces come within 0.1 lattice spacing of each other. This can sometimes help prevent the breakdown of the calculations when the particle density is high and there is considerable clustering together of the particles. This Hookean force (on particle 1) is obtained using

$$\mathbf{F}_{Hook}^{p} = \mathbf{0}, h \geq \delta,$$

$$\mathbf{F}_{Hook}^{p} = -F_0(1 - h/\delta)\hat{\mathbf{R}}_{12}, h < \delta. \quad (31)$$

The constant $F_0$ can be adjusted to control the magnitude of the repulsive force and the cut-off spacing $\delta = 0.1$. We use a value of $F_0 = 10$. In actual colloidal suspensions, additional forces between colloidal particles are present and these can be added in the model if required.

### F. Calculation of macroscopic variables (density and velocity)

At external fluid nodes outside the particles, this step is essentially similar to that described by Eqs. (3) and (4). However, some modifications are introduced for the fluid inside the particles. The density is still calculated via Eq. (3), but the velocity at each node inside the particle is assigned a value equal to the particle velocity, similar in form to Eq. (24). Thus, the fluid inside the particle is forced to assume a rigid-body motion corresponding to the particle. In addition, to remove the effects of the sound propagation in the interior fluid inside each particle, the average density inside each particle is calculated and the density at each node inside that particle is reset to the average density, as in Ref. [7]. This operation conserves mass and eliminates density fluctuations in the interior fluid. Because of the interior fluid, the density and velocity are not recalculated while evaluating forces due to the changing representation of the particle on the lattice (Sec. III B).

The calculations described in Sec. III A to Sec. III F are repeated until the system reaches a steady state or until the desired transient behavior is simulated. For two-phase problems where suspended particles are introduced near liquid drops, the liquid phase is allowed to reach equilibrium with the vapor phase before particle dynamics begins. This initial
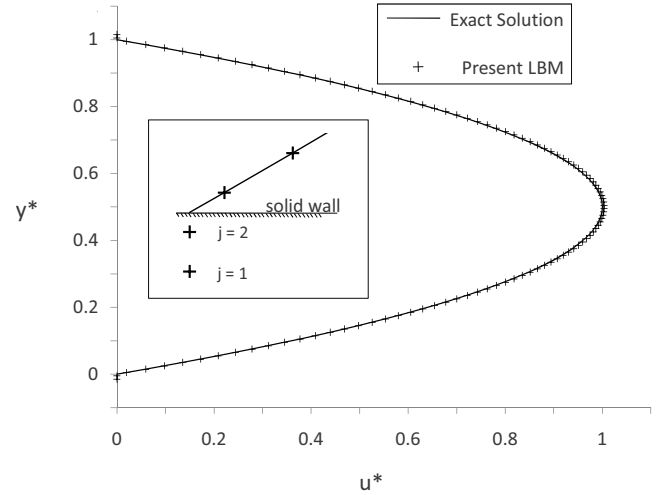


FIG. 2. Validation of the LBM with an exact solution to the Navier-Stokes equations for the case of body-force-driven Poiseuille flow in an infinite 2D channel. The velocity is normalized by the maximum velocity and the distance is normalized using the channel height. The inset shows the placement of lattice nodes and the velocity profile relative to the fixed wall ($y^* = 0$) at the bottom of the channel.

equilibration can take several thousand time steps but may be important to reduce effects of the initial condition on the subsequent particle dynamics [34].

## IV. MODEL VALIDATION

### A. Single-phase model without suspended particles

The exact difference method [25] used in the present LBM for incorporating external forces was validated against the exact solution to the Navier-Stokes equations for Poiseuille flow in an infinitely long 2D channel. In this problem, the top and bottom walls of a channel at $y = 0$ and $y = H$ are at rest and the flow is driven by a constant body force ($\mathbf{F}_{body} = g_x \mathbf{i}$) along the $x$ direction. The fluid density and dynamic viscosity are $\rho$ and $\nu$, respectively. At steady state, the flow profile is parabolic, with the maximum velocity at the centerline of the cavity given by $U_{max} = g_x H^2/(8\mu)$. Defining the normalized velocity $u^* = u/U_{max}$ and the dimensionless distance from the bottom plate $y^* = y/H$, the steady-state velocity profile is given by $u^* = 4y^*(1 - y^*)$.

We simulate this problem in the LBM using a $11 \times 105$ lattice with periodic boundaries along the $x$ direction and fixed solid nodes at $j = 1$, $j = 2$ and $j = 103$, and $j = 104$ representing the bottom and top walls. Based on the half-way bounce back rule used, the channel height $H = 100$. Other parameters in the LBM (in lattice units) are $g_x = 1/100000$, $\rho = 2.54$, and $\tau = 0.9$. Based on the relaxation time $\tau$, the kinematic viscosity $\nu = (2\tau - 1)/6 = 0.1333$. The dynamic viscosity $\mu = \rho\nu = 0.3386$ and $U_{max} = 0.0369$. The steady-state velocity profile obtained using the LBM is first normalized (using H = 100 and $U_{max} = 0.0369$) to make it dimensionless and then compared with the exact solution given above. Figure 2 shows that an excellent agreement between the LBM and the exact solution is obtained. The inset in Fig. 2 shows

the placement of the lattice nodes near the bottom wall. Note that there is no node at the precise location of the wall, but the no-slip boundary condition is enforced between the lattice nodes on either side of the wall between j=2 and j=3. The LBM simulations were repeated for relaxation times in the range $0.6 < \tau < 1.5$, and an excellent agreement with the analytical solution was obtained for all cases. The only constraint is that the LBM velocity (in lattice units) should be small compared to the speed of sound $c_s = 1/\sqrt{3}$ (in lattice units). This ensures that the simulations take place in the incompressible flow regime. In practice, accurate solutions for the incompressible flow can be obtained for $0 < U_{max}/c_s < 0.1$, beyond which the LBM can become unstable.

### B. Multiphase model without suspended particles

The SCMP model was used to study the phase-separation process of an initially single-phase fluid into distinct liquid and vapor phases. The driving mechanism of this phase separation is the cohesive force between fluid molecules located at adjacent lattice nodes. The simulation was carried out for a fluid on a periodic domain with an initially uniform density of 0.693 (corresponding to $\rho_c$). At time $t=0$, a small ($\pm 0.5\%$) perturbation is introduced in the density. As expected from the equation of state, if the cohesive force is less than a critical value ($g_f < -4/9$), these density perturbations grow with time and successively coarser liquid structures are formed throughout the domain. The density ratio between the liquid and vapor phases and the interface tension $\sigma^{liq\text{-}vap}$ between the two phases are controlled by the cohesive force parameter $g_f$. These simulations are useful in tabulating equilibrium liquid and vapor densities for various cohesive factors. The equilibrium densities can be used as initial conditions for subsequent simulations that start directly with a finite-sized liquid drop surrounded by the vapor phase. In the original Shan and Chen model [14], the equilibrium liquid and vapor densities change with the relaxation time $\tau$ even if $g_f$ is constant. The effect of $\tau$ on the density ratio is eliminated by using the exact difference method [25]. To calculate the interface tension $\sigma^{liq\text{-}vap}$, we measure the pressure difference $\Delta P$ inside and outside a liquid drop of radius $R$ in equilibrium with vapor for different drop sizes. This pressure difference is related to the interface curvature via the Laplace equation

$$\Delta P = \frac{\sigma^{liq\text{-}vap}}{R}. \qquad (32)$$

Depending on the radius of the drop, the pressure field takes up to 50000 lattice time steps or more to stop oscillating and reach steady state. Pressure measurements are taken after a steady pressure profile is obtained along the line through the drop center indicated by AB in Fig. 3(a). There are large fluctuations in the pressure distribution near the liquid-vapor interface. These fluctuations are an artifact caused by the sharp increase in density and are ignored while calculating the pressure difference. A typical example of the density and pressure distributions for $R=75$ is also shown in Fig. 3(a) (insets). At equilibrium, the average pressure inside the liq-
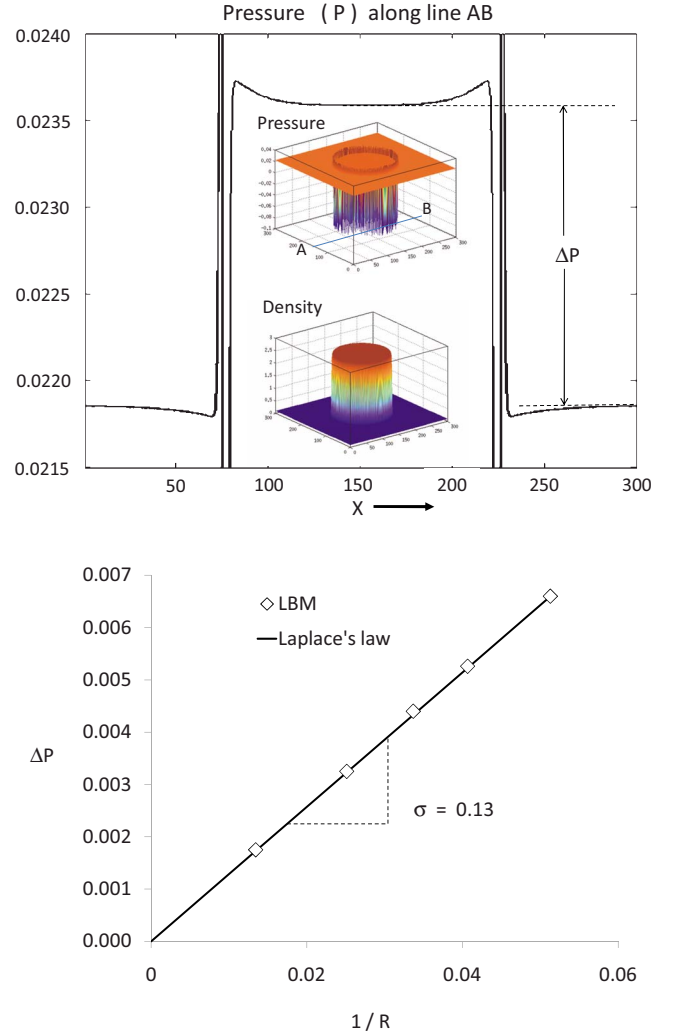




FIG. 3. (Color online) Using Laplace's law to obtain the interface tension in the LBM model using a $300 \times 300$ periodic lattice with $g_f = -0.65$. (a) Pressure and density distribution for a liquid drop with radius $R=75$. The density ratio is 30. (b) Summary of LBM results for drops of different radii and calibration of the interface tension $\sigma^{liq\text{-}vap}$ using Laplace's law. The solid line is drawn assuming $\sigma^{liq\text{-}vap}=0.13$.

uid drop (away from the interface) is slightly larger than the pressure outside it by an amount $\Delta P$. Based on Eq. (32), the slope of the line in a plot of $\Delta P$ versus the curvature of the liquid drop, as shown in Fig. 3(b), gives the interface tension. For the simulations in Fig. 3, $g_f = -0.65$ (this leads to $\rho_{liq}=2.53$ and $\rho_{vap}=0.08$) and $\sigma^{liq\text{-}vap}=0.13$.

Next, using the SCMP model, we calculate the equilibrium contact angle $\theta$ for a liquid drop on a perfectly flat and uniform substrate [inset in Fig. 4(a)]. The contact angle is related to the liquid-solid interface tension $\sigma^{liq\text{-}sol}$, the vapor-solid interface tension $\sigma^{vap\text{-}sol}$, and the liquid-vapor interface tension $\sigma^{liq\text{-}vap}$ via Young's law,

$$\cos(\theta) = \frac{\sigma^{liq\text{-}sol} - \sigma^{vap\text{-}sol}}{\sigma^{liq\text{-}vap}}. \qquad (33)$$

In the LBM, the contact angle can be changed by varying the adhesive force parameter $g_w$. Note that the density ratio be-
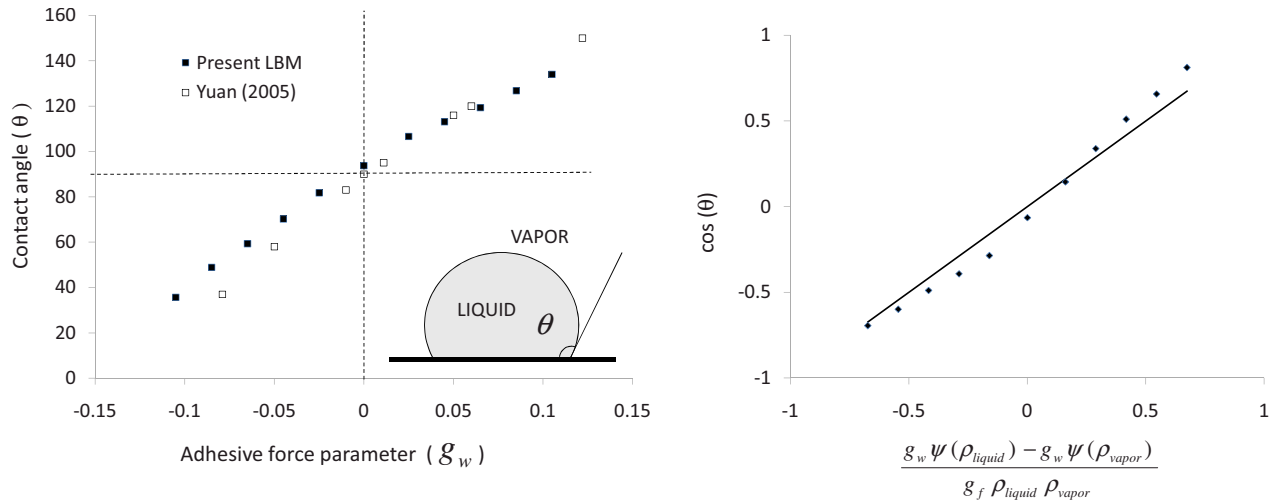
FIG. 4. (Color online) LBM simulation of different contact angles. (a) Comparison of the present LBM results with the 3D results of Yuan [35]. (b) Correlation of LBM results based on Eq. (34) for approximating interfacial tension parameters for use in the Young-Dupré relationship. The data points denote LBM results and the solid line is assuming that Eq. (34) holds exactly.

tween the liquid and vapor phase is still controlled by the cohesive force parameter, which is set to $g_f = -0.65$. The 2D results using the present LBM and similar results for a three-dimensional (3D) LBM implementation by Yuan [35] are compared in Fig. 4(a). The trend of the results is comparable, but some deviations are observed, especially for $g_w < 0$. The contact angle plug in from IMAGEJ [36] was used for measuring contact angles. The deviations may be due to differences in the wall density contribution to the adhesive force and in the density ratio used, the details of which are not fully disclosed by Yuan [35]. A direct comparison of the LBM results with Eq. (33) cannot be made because of the difficulty in obtaining the interface tension values $\sigma^{liq\text{-}sol}$ and $\sigma^{vap\text{-}sol}$ directly from the adhesion parameters. Huang *et al.* [37] recently proposed an empirical scheme for determining contact angles directly from the LBM adhesion parameters for a multicomponent system. Their results are not directly applicable to the current multiphase system; but on a similar note, we propose the following empirical relationship for the current multiphase system:

$$\cos(\theta) = \frac{g_w \Psi(\rho_{liq}) - g_w \Psi(\rho_{vap})}{g_f \rho_{liq} \rho_{vap}}. \tag{34}$$

In Fig. 4(b), we plot the left-hand and right-hand sides of Eq. (34) to show that the empirical correlation introduced above gives results that are reasonably accurate. Thus, estimates of the relevant interface tension values can be obtained by comparing Eq. (34) with Eq. (33). We note that the liquid-vapor interface tension obtained in Fig. 3(b) for the same set of parameters is close to the denominator in Eq. (34), indicating that the order of magnitude of the predictions for the liquid-solid and vapor-solid interface tensions in the numerator of Eq. (33) will be of comparable accuracy. A more thorough analysis of this empirical relationship or some alternative expressions to predict the contact angle in a multiphase LBM will be useful but are beyond the scope of this work.

### C. Particle suspension model in a single-phase fluid

To validate the LBM model of the force exerted on a moving particle, we have carried out a series of simulations for calculating the drag force $F_D$ exerted on a nonrotating circular cylinder of diameter $D$ moving with a uniform velocity $U$ through a single-phase fluid of density $\rho$. The fluid is bounded by two parallel walls at the top and bottom and the moving cylinder is located exactly in the middle of these walls [inset in Fig. 5(a)]. The results have been quantified by plotting the drag coefficient $C_D = 2F_D/(\rho U^2 D)$ as a function of the Reynolds number based on the particle diameter Re $= UD/\nu$. The Reynolds number was varied by changing the velocity of the suspended particle (along the $x$ axis) from 0.00375 to 0.12. The diameter of the moving particle was $D = 25$ and the width of the channel in the vertical direction was $L = 100$. The effect on the drag coefficient of periodic boundaries along the direction of motion of the particle can be reduced by increasing the lattice size along that direction. We used lattice sizes ranging from $1200 \times 100$ for low Re to $3000 \times 100$ for higher Re. In Fig. 5(a), the results for the drag coefficient from the LBM are compared with the results of Feng *et al.* [38] (for $L/D = 4$) and the LBM predictions are close to the published values for small Re but seem to deviate for large Re. The case $L/D = 4$ was also solved via the more accurate bounce back scheme for curved boundaries [29], using the linear interpolation. This improved the LBM predictions compared to the half-way bounce back rule. Simulations were also carried out for $L/D = 30$ and the LBM results were compared with the data of Sucker and Brauer [39]. It can be seen from Fig. 5(a) that the agreement is good for low Re but not so good for high Re. This discrepancy at large Re is mainly because of the effect of periodic boundaries and can be reduced by using a larger lattice size along the cylinder motion. Note that the motion of the cylinder is externally constrained to maintain a strictly uniform velocity and the force exerted by the fluid is decoupled from the suspended particle dynamics. To validate the calculation of the torque exerted by the fluid on a rotating particle, we
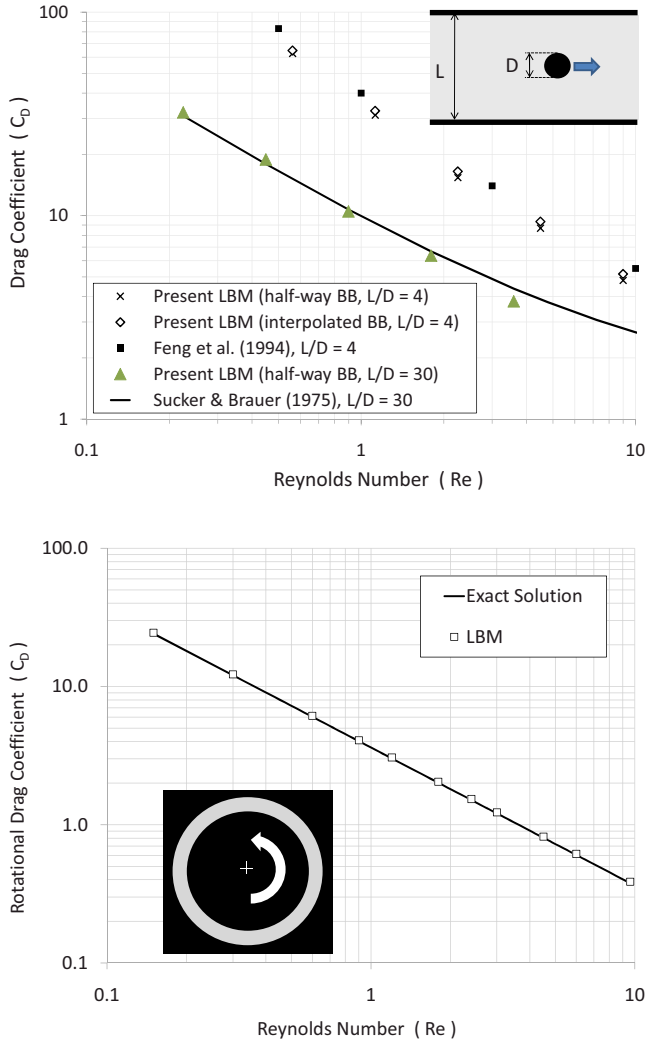
FIG. 6. Dynamics of an initially rotating particle (of radius $R$ = 15) coming to rest within a liquid phase is simulated using the implicit scheme. The angular velocity is normalized by its initial value. LBM parameters used are $300 \times 300$ periodic lattice, $g_f$ = −0.65, $g_w$ = −0.04, $\rho_{liq}$ = 2.53, and $\rho_p$ = 5.

### D. Coupled particle and fluid dynamics

Thus far, although the particle moved or rotated in the fluid, the force or torque exerted by the fluid on the particle (verified to be accurately calculated in the previous sections) was not allowed to play a role on the dynamics of the particle via Eqs. (11) and (12). This restriction is now relaxed. We validate the two-way dynamic coupling scheme using two simple problems. In the first problem, the particle is initialized in the liquid phase and is given an initial angular velocity. The resultant torque exerted by the liquid is allowed to influence the rotational dynamics, as described by Eq. (12). Because the particle is circular, the rotation does not change the representation in the particle on the lattice and numerical artifacts in the particle dynamics related to changing the particle representation on the lattice are eliminated. It is expected that the angular velocity reduces smoothly until the particle stops rotating. If the explicit scheme is used, the rotational dynamics is very sensitive to the density of the particle. For low particle density values, there are severe oscillations in the torque exerted by the fluid and the calculations are not stable. Stability can be recovered only for excessively large particle density values. The improved treatments for curved boundaries, while improving the accuracy of the bounce-back rule, do not reduce the instability in the rotational dynamics. In contrast, an implicit scheme (Appendix) allows any particle density to be used and the calculations remain stable. In Fig. 6, we plot the particle angular velocity as a function of time for a LBM simulation using the implicit scheme. Because of the inherent complexities in using the implicit scheme for a dense suspension, where particles can interact significantly with each other, we limit most of the subsequent results to situations where the problem contains some special symmetry such that rotational dynamics of suspended particles can be neglected.

In the second problem (inset in Fig. 7), we assign a linear initial velocity $[U(t=0)=0.05]$ to a particle located in the fluid such that it is midway between the stationary walls at the top and bottom of a $101 \times 105$ lattice. The channel height



FIG. 5. (Color online) Validation of the LBM model for (a) the drag force exerted by a single-phase fluid on a moving cylinder and (b) the frictional torque on a rotating cylinder.

carried out a series of LBM calculations using a $300 \times 300$ lattice for a particle of radius $R_1 = 100$ located at (150, 150) and enclosed within a fixed concentric cylindrical enclosure of radius $R_2 = 110$ [see inset in Fig. 5(b)]. The annular gap in between was filled with a single-phase fluid of density 0.693. The particle was then rotated about its center at a constant angular velocity $\Omega$ and the torque $T$ exerted by the fluid on the rotating particle was measured. Based on the solution of the Navier-Stokes equations for viscous flow between concentric cylinders, an exact analytical solution for the torque exerted on the cylinder is given by Donnelly and LaMar [40] as $T = 4\pi\mu R_1^2 R_2^2 \Omega / (R_2^2 - R_1^2)$. The LBM predictions have been compared with the exact solution by plotting the rotational drag coefficient $C_D = 2T/[\rho(R_1\Omega)^2(2R_1)^2]$ as a function of the *gap Reynolds number* Re $= R_1\Omega(R_2-R_1)/\nu$ and the results are shown in Fig. 5(b). The LBM prediction of the torque acting on the rotating cylinder matches closely with the exact analytical result.
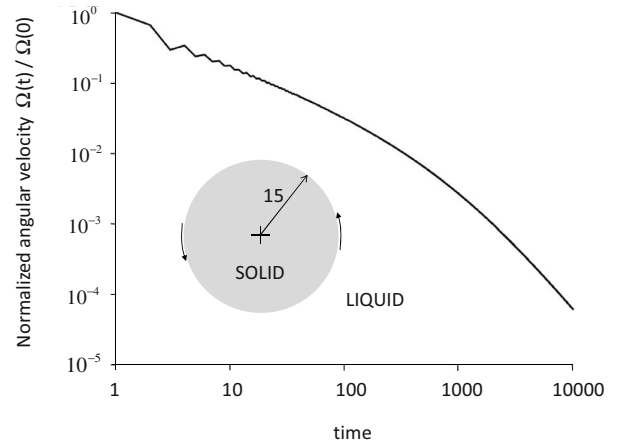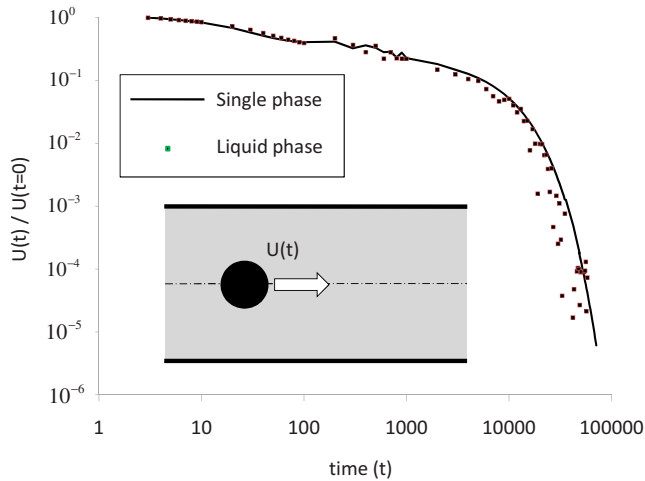
FIG. 7. (Color online) Dynamics of a single particle of radius $R=15$ set in motion inside a liquid with an initial (linear) velocity $U(t=0)=0.05$. The solid line represents the velocity decay for the single-phase problem and the data points represent the velocity decay for the liquid phase (with cohesive and adhesive forces present). The fluid density in both cases is 2.54 and the particle density is 5. The particle is initialized at the center of a $100\times100$ domain with periodic boundaries on the left and right and solid walls on the top and bottom.
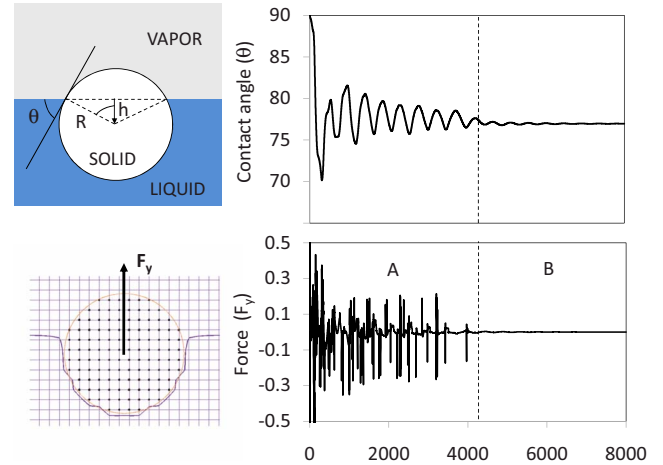


FIG. 8. (Color online) Dynamic response of a single particle suspended at a liquid-vapor interface. The particle is initially placed relative to the interface such that the contact angle is $\approx90°$ (neutral wetting). The particle then adjusts its vertical position relative to the interface depending on the adhesive force parameter and oscillates until it attains equilibrium. In this case, the final equilibrium position of the particle corresponds to $\theta\approx77°$. A transient analysis of the force acting on the particle reveals two distinct regions: region A where particle representation on the lattice changes (causing large fluctuations in the force) and region B, where it no longer changes (eliminating force fluctuations).

is 100. The symmetric location of the particle with respect to the top and bottom walls justifies neglecting the rotational dynamics and assuming a purely translational motion. It was confirmed using the implicit scheme that if the initial angular velocity is zero, it subsequently remains zero. Ideally, the initial linear velocity should reduce smoothly to zero because of the drag force exerted by the fluid. Figure 7 plots the transient velocity of the particle normalized using its initial value as it moves along the positive $x$ axis for two cases. The solid line in Fig. 7 is for a single-phase fluid with a fluid density of 2.54. For this case, it is found that the velocity of the particle reduces smoothly and exponentially with time. Note that adhesive and cohesive forces are absent for this single-phase case. Next, we consider the fluid to be the liquid phase of a multiphase system (without the vapor phase) and having the same density as the single-phase case. This result is indicated by the data points in Fig. 7. It is seen that although the velocity reduces with time with a comparable decay rate as the single-phase solution, there are considerable fluctuations. These fluctuations are thought to arise because the cohesive forces between (external) fluid nodes and adhesive forces between external fluid nodes and particle (internal fluid) nodes are affected significantly by the changing representation of the particle on the lattice. Reducing or eliminating these fluctuations will be a useful improvement of the present model and is under investigation.

## V. RESULTS AND DISCUSSION

### A. Single particle at the liquid-vapor interface

We first simulate the dynamics of a single nonrotating particle located at a flat liquid-vapor interface (Fig. 8). Body

forces like gravity are neglected in this simulation. Because of the inherent symmetry, rotational dynamics can be ignored in the subsequent motion of the particle, if the primary direction of motion is perpendicular to the interface. It is well known that the interface is a region of minimum energy [41] and that a particle suspended on the interface tends to attain a position relative to the interface corresponding to its equilibrium contact angle [42]. The equilibrium particle position relative to a perfectly flat interface can be uniquely defined by the distance ($h$) of the particle center from the interface. Based on particle radius $R$, the particle contact angle $\theta$ as defined in Fig. 8 (top left) can be calculated using $\theta=\cos^{-1}(h/R)$. This angle can also be estimated by using Young's law [Eq. (33)]. Similar to a liquid drop contacting a flat substrate, the liquid can be said to exhibit wetting behavior relative to the particle if $\theta<\pi/2$ and non wetting behavior if $\theta>\pi/2$. This wetting property can be controlled by the adhesive force parameter $g_w$, which can be independent of that used for fixed walls.

In the LBM simulations, the cohesive and adhesive force parameters were $g_f=-0.65$ and $g_w=-0.04$, respectively. The particle density $\rho_p=5$ and particle radius $R=6$. The lattice size used was $30\times100$, with a solid wall located at the bottom of the domain. This wall was used primarily to anchor the entire liquid layer on one side. The liquid phase was initialized as a 50-unit-thick layer above the solid wall. The other half of the domain was vapor. The initial location of the center of the particle was such that the contact angle was 90° (neutral wetting). The relaxation time $\tau=1$. Periodic conditions were used at the left and right boundaries. It is expected that the particle will change its vertical position relative to the interface because of the forces acting on it, eventually,
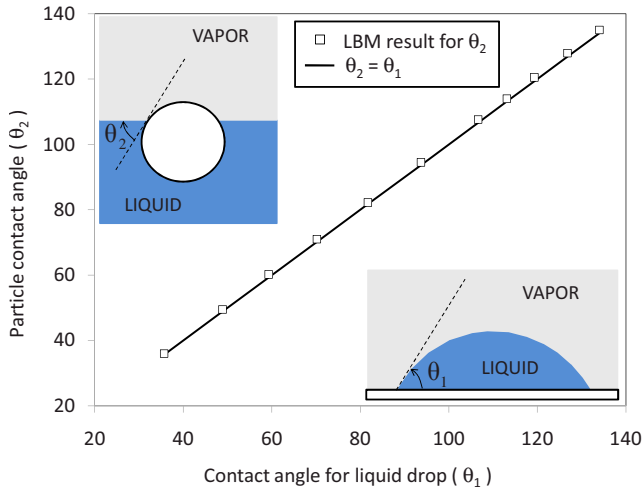
FIG. 9. (Color online) Lattice Boltzmann simulation of different particle contact angles ($\theta_2$) for a solid particle located at its equilibrium position at a liquid-vapor interface (inset, top left). For a given set of cohesive and adhesive force parameters, the particle contact angle and the equilibrium contact angle for a liquid drop ($\theta_1$) (inset, bottom right) are almost identical.

attaining an equilibrium position relative to the interface close to the equilibrium contact angle.

The dynamic response of the particle to the forces acting on it is shown in Fig. 8, which plots the particle contact angle and the force acting on the particle in the vertical direction with time. The particle initially oscillates considerably in the vertical direction around a position close to the equilibrium position. These oscillations are mainly because of the discrete manner in which the particle is represented on the lattice (bottom left in Fig. 8). Eventually, fluid viscosity damps these oscillations and after a certain point in time, the particle representation on the lattice no longer changes with time. The LBM calculations then rapidly attain a steady state. This explains the sudden reduction in force fluctuations observed in Fig. 8. For a low particle density, the particle responds rapidly to the forces acting on it. For a larger particle density, the particle responds more slowly to the forces exerted on it and the oscillations—while smoother—take longer to reach a steady value. In this case, the final equilibrium contact angle of the particle is approximately 77°. This result can be compared with the contact angle for a liquid drop resting on a flat substrate shown in Fig. 4(a). Because the same set of adhesive and cohesive force parameters have been used in Figs. 4(a) and 8, the contact angles for these cases should be the same. To check whether contact angles between these two cases are the same in general, we carried out LBM simulations for a particle with different wetting strengths. Figure 9 shows that for the same set of cohesive and adhesive force parameters, the particle contact angle is identical to the contact angle for a liquid drop resting on a flat substrate. Thus, the particle contact angle for wetting strength $g_w$ can be deduced from the simpler wetting problem of Fig. 4(a). Note that for all particle contact angles, the liquid-vapor interface is perfectly flat when the particle reaches an equilibrium position. This observation is consistent with the recent study of Onishi *et al.* [21], for the case
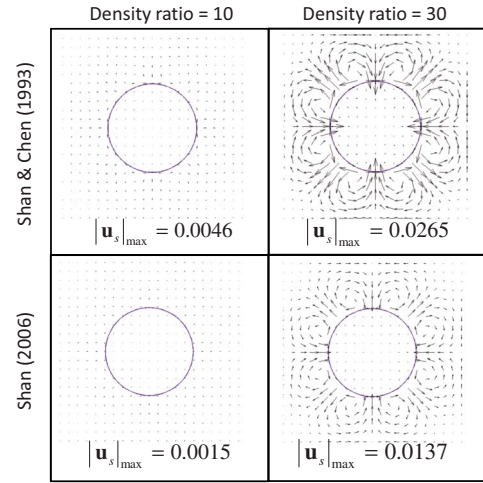


FIG. 10. (Color online) The spurious velocity field for a liquid drop (solid circle) at equilibrium with its vapor phase in the absence of suspended particles for two different density ratios (10 and 30) and using two different multiphase models Shan and Chen [14] and Shan [28].

where the bond number is zero. The effects of gravity have been neglected in the present work because the motivation was to study suspensions in micron-size drops where the bond number is very low.

## B. Effect of spurious currents on suspended particles near the interface

We next present a case where a single liquid drop and a suspended solid particle are close enough to interact. The liquid-vapor interface is known to be a region of minimum energy [41] and thus suspended particles will tend to be attracted to it. Because of the symmetry, it is justified to ignore the rotational dynamics of the particles for the ideal case where particles move toward or away from the liquid drop along a straight line. Spurious velocity currents near the interface (without suspended particles) are first examined for their possible role in the particle dynamics close to the interface. The LBM simulations are carried out using a 100 × 100 lattice with $g_w=0$ and $\tau=1$. A circular liquid drop of radius 25 is centered at (50, 50) and is initially at rest. In Fig. 10, the spurious velocity field when the liquid drop reaches equilibrium with its vapor phase is shown for two different density ratios 10 and 30, corresponding to $g_f=-0.54$ and $g_f=-0.65$, respectively, and for two different models, the original Shan and Chen model [14] and the recent model of Shan [28]. For all cases, it is found that in the vapor phase, there is a flow toward the liquid drop at the equator and at the north and south poles, while the flow is away from the liquid drop at angles of ±45° from the horizontal. The magnitude of the spurious velocity is larger for higher-density ratios. For a given density ratio, the spurious velocity currents can be reduced by using the improvements suggested by Shan [28]. To demonstrate the effects of spurious currents on suspended particles, the case with the maximum spurious currents is selected (top right in Fig. 10).
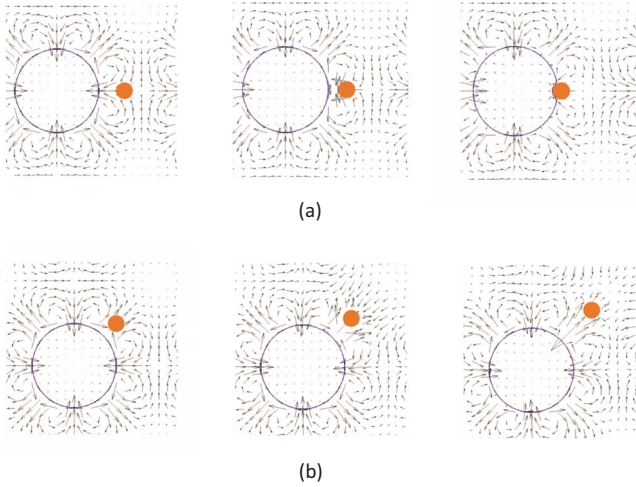
FIG. 11. (Color online) Effect of spurious velocity currents in the vapor phase on the dynamics of suspended particles (filled circles) located close to the liquid-vapor interface of a liquid drop (large circle). (a) A suspended particle located in the vapor phase at an angular location of 0° relative to the horizontal line from the drop center is attracted toward the liquid drop and (b) a suspended particle located at 45° is repelled from the liquid drop.
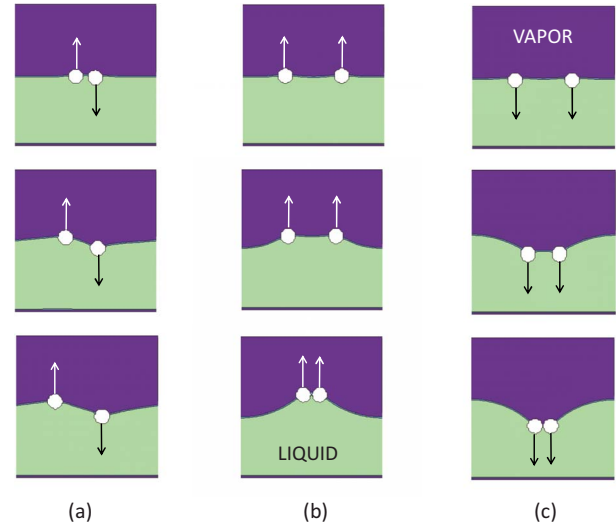


FIG. 12. (Color online) LBM simulation of two particles on an initially flat liquid-vapor interface subject to external forces. (a) Oppositely directed external forces cause the particles to drift apart. (b) Unidirectional external forces (toward vapor phase) cause the particles to move toward each other. (c) Uni-directionsl forces (toward the liquid phase) cause particles to move toward each other.

In Fig. 11, the liquid drop of radius 25 is initialized at (30, 50) in a $101 \times 101$ lattice (with periodic boundaries) and allowed to attain a steady equilibrium with the vapor phase. Particles are then introduced using two different initial configurations. In Fig. 11(a), a solid particle ($\rho_{particle}=5$) of radii $R=4.8$ is initially located at the coordinates (70, 50) in the vapor phase and is at rest. As the system evolves with time, it is observed the solid particle is attracted toward the liquid drop. When the liquid drop contacts the moving particle, the particle is drawn into the liquid-vapor interface and the liquid creeps along the particle surface. The initial momentum of the impact leads to some overshoot beyond the equilibrium contact angle, but the system soon attains a steady state where the liquid drop and the solid particle embedded in the liquid-vapor interface both attain a fixed spatial position. The liquid-vapor interface reattains its circular shape at steady state. Note that the initial and final momentums of the system are identical as the liquid drop and particle are at rest at both times. This result seems to be consistent with the validation of the conservation of linear momentum in the LBM algorithm. Unfortunately, this seemingly accurate prediction is a result of the spurious velocity field in the vapor phase, which is directed toward the liquid drop in the vicinity of the suspended particle. If the initial particle location is rotated relative to the center of the liquid drop such that it is at an angle of 45° to the horizontal, the LBM calculations lead to a completely different result [Fig. 11(b)], where the particle is repelled from the liquid drop instead of getting attracted to it. Again, this can be understood by looking at the nature of the spurious velocity field outside the curved interface, as shown in Fig. 10.

When the solid particles are initialized such that they touch the liquid-vapor interface, the particles remain attached to the interface. The particle and the liquid drop then merely adjust their relative positions such that the equilibrium contact angle is attained. This indicates that the LBM is qualitatively accurate in predicting the interface as a region of the minimum energy. Removing these unphysical effects due to spurious currents is one of the challenges for further research in this area. In the mean time, using a lower density ratio or implementing the more isotropic model of Shan [28] is helpful in reducing the magnitude of these effects.

## C. Capillary interactions between particles located on a flat liquid-vapor interface

Next, we examine the behavior of two particles of the same size that are initially located on a flat liquid-vapor interface and are subsequently subjected to different external forces in the vertical direction. The liquid layer has a depth of 50, with a solid wall close to the bottom of the domain (to anchor the liquid layer) and the particle diameter is 4.8. The lattice size used is $100 \times 100$, with periodic boundary conditions on the left and right boundaries. The cohesive force $g_f=-0.65$ (liquid-vapor density ratio $\approx 30$), the adhesive force $g_w=-0.04$, and $\tau=1$ in both the liquid and vapor phases. The particle density $\rho_{particle}=5$. The initial condition specifies zero velocity for all particles and for the liquid and vapor phases. The two particles are initially located such that their equator is slightly below the liquid-vapor interface. For the first case shown in Fig. 12(a), the initial (center to center) spacing between the two particles is 14 and the vertical forces on the two particles (0.06 units each) act in opposite directions, pulling the first particle up toward the vapor phase and the other particle down toward the liquid phase. It can be observed that the two particles drift apart under the action of these opposite forces. Because periodic boundary conditions are used, the particles spread apart until a roughly

uniform particle spacing is achieved. In Figs. 12(b) and 12(c), the initial (center to center) spacing between the particles is 40 and the external forces on both particles (0.1 unit) act in the same direction. In this case, the particle spacing is observed to reduce with time and the two particles eventually form a closely packed cluster at the center of the domain.

These results can be physically interpreted by imagining the liquid-vapor interface as an elastic string that passes through both particles while allowing them to slide over the string. In the first case (opposite forces), the external forces pull the particles apart until a minimum-energy configuration is reached where the system is in equilibrium. Similarly, in Figs. 12(b) and 12(c), the minimum-energy equilibrium configuration is attained when both particles are almost in contact (kept slightly apart because of the lubrication and Hookean forces) and the interface is pulled up and down, respectively, to balance the external forces. The forces acting on the particles have to be smaller than a critical value in order to avoid detaching the particle from the liquid-vapor interface. These results are qualitatively consistent with Onishi *et al.* [21], who simulated the lateral motion driven by the capillary interaction between two particles on a binary interface. The present model is also able to successfully simulate the related *immersion* problem [43], where two particles are attracted toward each other in a thin liquid film wetting a substrate. The effect of rotational dynamics on these results needs to be included for a more realistic simulation.

### D. Spinodal decomposition in the presence of suspended particles

The effect of suspended particles on the spinodal decomposition process was recently studied by Stratford *et al.* [19,20] in the context of demixing of a binary liquid mixture. Interesting effects, such as colloidal jamming, have been observed, where the suspended particles are sequestered in the fluid-fluid interfacial region and thus prevent or markedly reduce the decomposition of a binary mixture. We have carried out a similar study for the present multiphase system using a $300 \times 300$ lattice with periodic boundaries. It is necessary to use virtual images of each particle in adjacent periodic domains during the calculations. This is required to check if a pair of particles is close enough to interact across periodic boundaries or when a particle intersects with the edges of the lattice and consequently has to reappear, in part, at the opposite edge. The initial condition is an array of 36 suspended particles of radius $R=4.8$ (3% volume fraction) arranged in the form of a regular equally spaced $6 \times 6$ array of rows and columns (Fig. 13). All particles are initially at rest and are surrounded by a fluid phase that is initially at a uniform density of 0.693. Other parameters used are $g_f=-0.65$ (liquid-vapor density ratio $\approx 30$), $g_w=-0.04$ (corresponding to a 77° equilibrium contact angle), $\tau=1$, and $\rho_{particle}=5$. At time $t=0$, the fluid density is randomly perturbed by $\pm 0.5\%$ and these perturbations then grow because of the mutual cohesive attraction and the fluid begins to separate into distinct liquid and vapor phases. However, the coarsening process driven by the tendency of reducing the
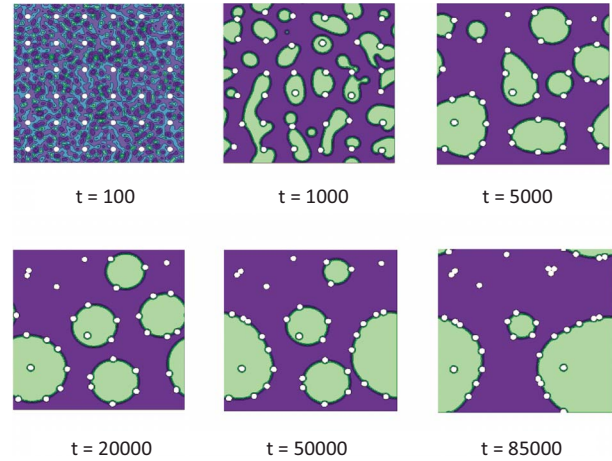


FIG. 13. (Color online) LBM simulation of spinodal decomposition in the presence of suspended particles. The particles are initially arranged in a uniform $6 \times 6$ array and are at rest. Subsequently, as the green (light gray) liquid domains begin to form and coalesce, the particles tend to accumulate at the liquid-vapor interface and inhibit coarsening of the interface.

liquid-vapor interfacial area is inhibited because of the suspended particles compared to the coarsening process without particles (not shown). These particles move to the liquid-vapor interfacial regions and several liquid drops with particles along the interface region can be observed. In the absence of Brownian motion, once trapped, particles will remain at the liquid-vapor interface during the coarsening process. Eventually, some of these liquid drops coalesce together, causing a further rearrangement of the particles on the interface. The accumulation of particles at the interface and the curtailment of coarsening observed here are very similar to those described in Stratford *et al.* [20] in the context of a binary mixture. However, unlike the neutrally wetting particles used in Ref. [20], the particles in the present study preferentially wet the liquid phase. Thus, qualitatively accurate results are obtained even when the rotational dynamics of particles is neglected. The effect of rotational dynamics should, however, be included for a more accurate simulation.

## VI. CONCLUDING REMARKS

In this paper, a two-dimensional multiphase LBM has been developed such that one or both phases (liquid and vapor) can have suspended solid particles dispersed within it. The suspended particles are circular in shape and are dynamically coupled to the fluid flow. The Shan and Chen model [14] has been used to simulate the two-phase flow and the particle suspension model pioneered by Ladd and co-workers has been modified to account for adhesive forces between the suspended particles and the liquid and vapor phases. The combined model has been extensively validated and found to be accurate and physically realistic, although there are some instability issues for two-phase scenarios related to force fluctuations when suspended particles move on the LBM lattice. Recently, an improved method for initializ-

ing new fluid nodes (uncovered by moving particles) and a corrected momentum exchange algorithm for calculating forces on suspended particles have been proposed [44,45]. These schemes do not consider adhesive and cohesive forces, but they might be useful in reducing the instability and are presently under investigation.

The results demonstrate the capability of the multiphase LBM to model complex fluid dynamic problems involving suspended solids. It is shown how a suspended particle located at the liquid-vapor interface attains a stable position corresponding to its wetting properties. The LBM confirms that the interface is a local energy minimum for suspended particles. Spurious currents have been shown to lead to unphysical effects, such as attraction or repulsion of freely suspended particles in the vapor phase to a liquid drop, depending on the angular position of the particle relative to the drop. These effects can be reduced, but not completely eliminated, by reducing the density ratio or by using more isotropic models [28]. Particle accumulation at the interface observed in the context of multicomponent fluid mixtures is also observed in the present multiphase scenario, as illustrated by the case of the spinodal decomposition in the presence of suspended particles.

The entire algorithm can be efficiently parallelized and extended to three dimensions. In many applications of colloidal drops settling onto a substrate, such as ink-jet-printed electronics, the suspended particle dynamics is influenced by flow fields within the liquid due to thermal gradients and because of additional long-range forces between the particles themselves. The effect of particle rotation dynamics also needs to be analyzed more carefully. Adding in these effects is a part of our ongoing effort and the results will be reported in a future publication.

### APPENDIX: IMPLICIT SCHEME FOR UPDATING LINEAR AND ANGULAR VELOCITY OF A SINGLE SUSPENDED PARTICLE

In this appendix, we extend and adapt the implicit scheme of Lowe *et al.* [6] to the particle suspension model described in this work. The basic idea is that the (unknown) particle velocity at the new time level is to be used in the expression for calculating the boundary velocity of the particle given by Eq. (24). Expressions for the forces and torques acting on the particle of mass $M$ and moment of inertia $I$ are first derived using the two (unknown) velocity components along $x$ and $y$ directions at the new time level denoted by $u$ and $v$, respectively, and the (unknown) angular velocity of the particle along $z$ direction at the new time level denoted by $\Omega$. Newton's second law is then applied to relate these forces (along

$x$ and $y$) and torque (along $z$) to the change in the linear and angular velocities of the particle. The result is a set of three linear equations that can be solved for the three unknowns. After some algebra, the resulting system of equations can be written as

$$
\begin{pmatrix} A_{11} & A_{12} & A_{13} \\ A_{21} & A_{22} & A_{23} \\ A_{31} & A_{32} & A_{33} \end{pmatrix} \begin{pmatrix} u \\ v \\ \Omega \end{pmatrix} = \begin{pmatrix} B_1 \\ B_2 \\ B_3 \end{pmatrix}. \tag{A1}
$$

The elements of the coefficient matrix are given by

$$
A_{11} = 1 + \frac{6}{M} \sum_{bn} \sum_{\alpha} \rho w_\alpha \mathbf{e}_{\alpha x} \mathbf{e}_{\alpha x}, \tag{A2}
$$

$$
A_{12} = A_{21} = \frac{6}{M} \sum_{bn} \sum_{\alpha} \rho w_\alpha \mathbf{e}_{\alpha y} \mathbf{e}_{\alpha x}, \tag{A3}
$$

$$
A_{13} = -\frac{6}{M} \sum_{bn} \sum_{\alpha} (\rho r_y w_\alpha \mathbf{e}_{\alpha x} \mathbf{e}_{\alpha x} - \rho r_x w_\alpha \mathbf{e}_{\alpha y} \mathbf{e}_{\alpha x}), \tag{A4}
$$

$$
A_{22} = 1 + \frac{6}{M} \sum_{bn} \sum_{\alpha} \rho w_\alpha \mathbf{e}_{\alpha y} \mathbf{e}_{\alpha y}, \tag{A5}
$$

$$
A_{23} = -\frac{6}{M} \sum_{bn} \sum_{\alpha} (\rho r_y w_\alpha \mathbf{e}_{\alpha x} \mathbf{e}_{\alpha y} - \rho r_x w_\alpha \mathbf{e}_{\alpha y} \mathbf{e}_{\alpha y}), \tag{A6}
$$

$$
A_{31} = -\frac{6}{I} \sum_{bn} \sum_{\alpha} (\rho r_y w_\alpha \mathbf{e}_{\alpha x} \mathbf{e}_{\alpha x} - \rho r_x w_\alpha \mathbf{e}_{\alpha y} \mathbf{e}_{\alpha x}), \tag{A7}
$$

$$
A_{32} = -\frac{6}{I} \sum_{bn} \sum_{\alpha} (\rho r_y w_\alpha \mathbf{e}_{\alpha x} \mathbf{e}_{\alpha y} - \rho r_x w_\alpha \mathbf{e}_{\alpha y} \mathbf{e}_{\alpha y}), \tag{A8}
$$

$$
A_{33} = 1 + \frac{6}{I} \sum_{bn} \sum_{\alpha} (\rho r_x r_x w_\alpha \mathbf{e}_{\alpha y} \mathbf{e}_{\alpha y} + \rho r_y r_y w_\alpha \mathbf{e}_{\alpha x} \mathbf{e}_{\alpha x}
$$
$$
- 2\rho r_x r_y w_\alpha \mathbf{e}_{\alpha x} \mathbf{e}_{\alpha y}). \tag{A9}
$$

The right-hand side of Eq. (A1) is calculated using

$$
B_1 = u_0 + \frac{2}{M} \sum_{bn} \sum_{\alpha} f_\alpha^+ \mathbf{e}_{\alpha x} + \frac{1}{M} \sum_{bn} \mathbf{F}_{adh,x}^p + \frac{1}{M} [\mathbf{F}_{U,x} + \mathbf{F}_{C,x}],
$$
$$
\tag{A10}
$$

$$
B_2 = v_0 + \frac{2}{M} \sum_{bn} \sum_{\alpha} f_\alpha^+ \mathbf{e}_{\alpha y} + \frac{1}{M} \sum_{bn} \mathbf{F}_{adh,y}^p + \frac{1}{M} [\mathbf{F}_{U,y} + \mathbf{F}_{C,y}],
$$
$$
\tag{A11}
$$

$$B_3 = \Omega_0 + \frac{2}{I}\sum_{bn}\sum_{\alpha}(r_x f_\alpha^+ \mathbf{e}_{\alpha y} - r_y f_\alpha^+ \mathbf{e}_{\alpha x})$$

$$+ \frac{1}{I}\sum_{bn}(r_x \mathbf{F}_{adh,y} - r_y \mathbf{F}_{adh,x})$$

$$- \frac{1}{I}\sum_{U}(r_{U,x}\bar{\rho}_U \mathbf{u}_{U,y} - r_{U,y}\bar{\rho}_U \mathbf{u}_{U,x})$$

$$+ \frac{1}{I}\sum_{C}(r_{C,x}\rho_C \mathbf{u}_{C,y} - r_{C,y}\rho_C \mathbf{u}_{C,x}). \qquad (A12)$$

In the above expressions, $u_0$, $v_0$, and $\Omega_0$ represent (known) values at the current time level. The summations are to be carried out over each boundary node ($bn$) and over all the relevant directions ($\alpha$) at that boundary node. The location of the relevant node point is denoted by $\mathbf{r}$. Subscripts $x$ and $y$ denote components along the $x$ and $y$ axes and subscripts $U$ and $C$ denote uncovered and covered nodes, respectively. Implementing this scheme requires two passes through the domain. During the first pass, the coefficients $A_{ij}$ and $B_i$ are assembled. After the linear system of equations, i.e., Eq. (A1) is solved, another pass through the domain is made to update the relevant PDFs based on the calculated values of $u$, $v$, and $\Omega$. The adhesive forces in $B_i$ are based on Eq. (28) and the forces because of changing particle representation on the lattice are calculated using Eqs. (17)–(20). The advantage of using the implicit scheme is that rotational dynamics can be included in the calculations without introducing the numerical instability. The scheme described here can be implemented for any number of suspended particles as long as the particles do not come too close to one another. If lubrication and Hookean forces between particles are to be included in the derivation of the implicit scheme, the implementation is much more complex due to the increase in the number of unknowns induced by particles that are *close enough* to influence each other (see Nguyen and Ladd [5] for more details). Another useful extension will be to incorporate interpolated bounce back into the implicit scheme for accurately describing interactions with curved boundaries. These extensions are still in progress and will be reported in a future publication.

[1] A. J. C. Ladd, J. Fluid Mech. **271**, 285 (1994).
[2] A. J. C. Ladd, J. Fluid Mech. **271**, 311 (1994).
[3] C. K. Aidun, Y. Lu, and E. J. Ding, J. Fluid Mech. **373**, 287 (1998).
[4] A. J. C. Ladd and R. Verberg, J. Stat. Phys. **104**, 1191 (2001).
[5] N. Q. Nguyen and A. J. C. Ladd, Phys. Rev. E **66**, 046708 (2002).
[6] C. P. Lowe, D. Frenkel, and A. J. Masters, J. Chem. Phys. **103**, 1582 (1995).
[7] M. W. Heemels, M. H. J. Hagen, and C. P. Lowe, J. Comput. Phys. **164**, 48 (2000).
[8] E. J. Ding and C. K. Aidun, J. Stat. Phys. **112**, 685 (2003).
[9] S. Ramachandran, P. B. Sunil-Kumar, and I. Pagonabarraga, Eur. Phys. J. E **20**, 151 (2006).
[10] J. Kromkamp, D. v. den Ende, D. Kandhai, R. van der Sman, and R. Boom, Chem. Eng. Sci. **61**, 858 (2006).
[11] C. Sun and L. L. Munn, Comput. Math. Appl. **55**, 1594 (2008).
[12] K. Stratford and I. Pagonabarraga, Comput. Math. Appl. **55**, 1585 (2008).
[13] A. K. Gunstensen, D. H. Rothman, S. Zaleski, and G. Zanetti, Phys. Rev. A **43**, 4320 (1991).
[14] X. Shan and H. Chen, Phys. Rev. E **47**, 1815 (1993).
[15] X. Shan and H. Chen, Phys. Rev. E **49**, 2941 (1994).
[16] M. R. Swift, W. R. Osborn, and J. M. Yeomans, Phys. Rev. Lett. **75**, 830 (1995).
[17] M. R. Swift, E. Orlandini, W. R. Osborn, and J. M. Yeomans, Phys. Rev. E **54**, 5041 (1996).
[18] G. Thömmes, J. Becker, M. Junk, A. K. Vaikuntham, D. Kerhwald, A. Klar, K. Steiner, and A. Wiegmann, J. Comput. Phys. **228**, 1139 (2009).
[19] K. Stratford, R. Adhikari, I. Pagonabarraga, and J. C. Desplat, J. Stat. Phys. **121**, 163 (2005).
[20] K. Stratford, R. Adhikari, I. Pagonabarraga, J. C. Desplat, and M. E. Cates, Science **309**, 2198 (2005).
[21] J. Onishi, A. Kawasaki, Y. Chen, and H. Ohashi, Comput. Math. Appl. **55**, 1541 (2008).
[22] X. He and L. S. Luo, Phys. Rev. E **56**, 6811 (1997).
[23] R. R. Nourgaliev, T. N. Dinh, T. G. Theofanous, and D. Joseph, Int. J. Multiphase Flow **29**, 117 (2003).
[24] M. Junk, A. Klar, and L. S. Luo, J. Comput. Phys. **210**, 676 (2005).
[25] A. L. Kupershtokh and D. A. Medvedev, J. Electrost. **64**, 581 (2006).
[26] R. Benzi, L. Biferale, M. Sbragaglia, S. Succi, and F. Toschi, Phys. Rev. E **74**, 021509 (2006).
[27] P. Yuan and L. Schaefer, Phys. Fluids **18**, 042101 (2006).
[28] X. Shan, Phys. Rev. E **73**, 047701 (2006).
[29] M. Bouzidi, M. Firdaouss, and P. Lallemand, Phys. Fluids **13**, 3452 (2001).
[30] P. Lallemand and L. S. Luo, J. Comput. Phys. **184**, 406 (2003).
[31] B. Chun and A. J. C. Ladd, Phys. Rev. E **75**, 066705 (2007).
[32] A. Caiazzo and M. Junk, Comput. Math. Appl. **55**, 1415 (2008).
[33] P. H. Kao and R. J. Yang, J. Comput. Phys. **227**, 5671 (2008).
[34] D. Qian, J. B. McLaughlin, K. Sankaranarayanan, S. Sunderesan, and K. Kontomaris, Chem. Eng. Commun. **193**, 1038 (2006).
[35] P. Yuan, Ph.D. thesis, University of Pittsburg, 2005.
[36] http://rsweb.nih.gov/ij/
[37] H. Huang, D. T. Thorne, M. G. Schaap, and M. C. Sukop, Phys. Rev. E **76**, 066701 (2007).
[38] J. Feng, H. H. Hu, and D. D. Joseph, J. Fluid Mech. **261**, 95 (1994).
[39] D. Sucker and H. Brauer, Waerme-Stoffuebertrag. **8**, 149 (1975).
[40] R. J. Donnelly and M. M. LaMar, Phys. Rev. A **36**, 4507

(1987).

[41] P. Pieranski, Phys. Rev. Lett. **45**, 569 (1980).

[42] H. J. Butt, K. Graf, and M. Kappl, *Physics and Chemistry of Interfaces* (Wiley-VCH, Berlin, 2003) p. 123.

[43] P. A. Kralchevsky and N. D. Denkov, Curr. Opin. Colloid In-

terface Sci. **6**, 383 (2001).

[44] A. Caiazzo, Prog. Comput. Fluid Dyn. **8**, 3 (2008).

[45] E. Lorenz, A. Caiazzo, and A. G. Hoekstra, Phys. Rev. E **79**, 036705 (2009).